The cathode material of a sodium ion battery, $Na_3V_2(PO_4)_2F_3$, undergoes Co/N-doped carbon modification using a bimetallic MOFs template

Junjie Ma[a], Wei Li[a,*], Xiaoqi Lan[a], Zheng Liu[a,*], Fenghai Zhou[a], Mingjun Lu[a]

and Guo-Cheng Han[b,*]

a. College of Chemical and Biological Engineering, Guilin University of Technology, Guangxi Key Laboratory of Electrochemical and Magneto-chemical Functional Materials, Guilin 541004, China.

b. School of Life and Environmental Sciences, Guilin University of Electronic Technology, Guilin 541004, China.

Abstract: The $Na_3V_2(PO_4)_2F_3$/Co/N-PC composite was prepared based on nitrogen-doped porous carbon materials containing cobalt (Co/N-PC), which is obtained through high-temperature pyrolysis of bimetallic Co/Zn-MOF. The electrochemical test results showed that the discharge specific capacity of $Na_3V_2(PO_4)_2F_3$/Co/N-PC composite was 126.66 mAh/g at 0.1C , an increase of 15.6% compared with $Na_3V_2(PO_4)_2F_3$/N-PC(109.56 mAh/g). The capacity retention rate was 91.84% after 100 cycles and the R_{SEI} of the $Na_3V_2(PO_4)_2F_3$/Co/N-PC composite (48.62 Ω) outperforms that of the $Na_3V_2(PO_4)_2F_3$/N-PC composite (81.55 Ω). This work applied the metal/carbon hybrid materials obtained through high temperature pyrolysis of bimetallic organic frameworks were employed in sodium-ion batteries, thereby offering enhanced potential for the advancement of sodium-rich phosphoric acid modified materials.

Key Words: $Na_3V_2(PO_4)_2F_3$; sodium-ion batteries; cathode materials; electrochemical performance

1 Introduction

The compound $Na_3V_2(PO_4)_2F_3$ has been reported to exhibit inadequate conductivity and ion diffusion rate, which is considered a crucial factor impeding its potential for enhancing rates and maintaining capacity in battery cathode material applications[1,2]. Therefore, addressing the enhancement of electrochemical performance in $Na_3V_2(PO_4)_2F_3$ has become an urgent imperative.

In recent years, considerable attention has been devoted to doping modification with transition

* Corresponding author.

E mail address: liwei1986gllg@163.com (W. Li), 609563181@qq.com (Z. Liu), hangc1981@163.com (G.-C. Han)

metals Fe[3], Co[4], Ni[5], and Mo[6] due to their capacity for augmenting electrical conductivity and furnishing additional active sites. However, the development of transition metal doping is still impeded by challenges such as the agglomeration of metal nanoparticles and the limited density of active sites[7-9]. In recent years, the unique structures and exceptional properties of metal-organic frameworks (MOFs) have garnered increasing attention, positioning them as a subject of significant interest in academic research [10-18]. The establishment of a well-defined structure is crucial in electro catalytic design, as it serves to mitigate excessive potential difference, facilitate reaction kinetics, and enhance energy efficiency[19,20]. Concurrently, a multitude of researchers have also discovered that MOFs can be employed for the synthesis of metal/carbon hybrid materials through pyrolysis techniques, thereby preserving the exceptional specific surface area characteristic of MOFs while demonstrating remarkable conductive and catalytic properties. The Co nanoparticles are embedded within the nitrogen-doped carbon layer in the nitrogen-doped carbon material, which is prepared using Co-MOFs as the precursor system, exhibiting excellent electro catalytic performance.

Zhao et al.[21] synthesized nitrogen-doped carbon materials incorporating Co nanoparticles via the pyrolysis of Co-MOFs, a novel three-dimensional molecular architecture. The multi-layered structure resembles sandwich-like nanocomposites, exhibiting enhanced performance in oxygen reduction reaction (ORR) and oxygen evolution reaction (OER). This improvement can be attributed to the synergistic effect between highly active and stable monodisperse cobalt nanoparticles and the porous N-doped carbon framework with excellent conductivity. Chen et al.[22] propose that the synergistic effect between cobalt and nitrogen optimizes both the adsorption energy of carbon by hydrogen atoms and the electronic structure of carbon, thereby enhancing catalytic activity and facilitating electron transfer during HER. The study conducted by Zitolo et al.[23] demonstrated the superiority of cobalt-based materials, with Co as the central metal atom, over iron-based materials containing other metals as the central metal atom (e.g., Fe) in terms of catalytic reaction sites and redox reaction rates. Xu et al.[24] developed a novel approach utilizing Co-Ni-MOF as a precursor for the synthesis of N-doped carbon composite $Co(Ni)Se_2$ three-dimensional materials via high-temperature selenization. The $Co(Ni)Se_2$@NCC (N-doped carbon composite) is synthesized, exhibiting a well-defined hollow diamond morphology attributed to the synergistic effect of bimetallic Co and Ni elements. The

2

nanoparticles of $CoSe_2$ and $NiSe_2$ are uniformly dispersed within an N-doped carbon shell. he cathode material of sodium ion battery, $Co(Ni)Se_2@NCC$, exhibits high reversible specific capacity, excellent rate and dynamic performance, as well as remarkable cycle stability. In summary, the utilization of novel Co-MOFs and their derivatives as modifiers holds great potential for enhancing the electrochemical properties of electrode materials[25].

In this study, we synthesized and pyrolyzed bimetallic Co/Zn-ZIF at high temperature to obtain porous nitrogen-doped carbon nanocubes containing cobalt nanoparticles (Co/N-PC), aiming to enhance the electrochemical properties of materials through the synergistic effect between cobalt nanoparticles and porous N-doped carbon materials. During the high temperature carbonization process, Co/Zn-ZIF undergoes a conversion where Zn is transformed into steam and subsequently released. Co^{2+} is reduced to Co nanoparticles through the catalytic action of reducing gases (NH_3 and H_2) generated during high-temperature pyrolysis. The incorporation of nano-sized Co into nitrogen-doped porous carbon materials can significantly enhance the electrical conductivity and facilitate charge transfer in electrode materials. The results also demonstrate that $Na_3V_2(PO_4)_2F_3$/Co/N-PC exhibits excellent electrochemical performance as a cathode material for sodium-ion batteries, characterized by stable charge and discharge profiles and prolonged cycling stability.

2 Experimental

2.1 Synthesis of $Na_3V_2(PO_4)_2F_3$/Co/N-PC composites

Ammonium dihydrogen phosphate ($NH_4H_2PO_4$), citric acid monohydrate ($C_6H_8O_7 \cdot H_2O$), methanol (CH_3OH) were purchased from Xilong Chemical Co., Ltd.; Methyl trimethylamine bromide (CTAB), 2-methylimidazole (2-MeIm), and ammonium metavanadate (NH_4VO_3) were purchased from Aladdin's Reagents (Shanghai Co., Ltd.); Zinc nitrate hexahydrate ($Zn(NO_3)_2 \cdot 6H_2O$), cobalt nitrate hexahydrate ($Co(NO_3)_2 \cdot 6H_2O$), Sodium fluoride (NaF), Sodium carboxymethyl cellulose (CMC), Sodium sulfate (Na_2SO_4) were purchased from Shanghai Mclean Biochemical Technology Co., Ltd.; Acetylene black was procured from Taiyuan Liyuan Lithium Battery Technology Center Co.; Anhydrous ethanol purchased from Tianjin Fuyu Fine Chemical Co., Ltd.; Anhydrous ethanol purchased from Tianjin Fuyu Chemical Co., Ltd. All the precursors were used directly.

3

The weighed amounts of 223.12 mg $Zn(NO_3)_2 \cdot 6H_2O$, 72.76 mg $Co(NO_3)_2 \cdot 6H_2O$, and 5 mg CTAB were dissolved in 10 mL deionized water with stirring for 5 min to form solution A. The weighed amounts of 4540 mg 2-MeIm were dissolved in 70 mL of deionized water with stirring for 5 min to form solution B. Subsequently, Solution A was quickly added to solution B, and was vigorously stirred at 25℃ for 20 min to obtain a lilac emulsion, which was then covered with plastic wrap at room temperature and aged for 24 h. Then it was centrifuged at 4000 r/min, washed with ethanol and deionized mixture ($V_{ethanol}$: V_{water} = 1:1) for 5-6 cycles, and finally dried in a vacuum drying oven at 60℃ for 12 h. The resulting sample was labeled as Co/Zn-ZIF.

The Co/Zn-ZIF purple powder sample was accurately weighed and transferred into the crucible. The temperature was gradually increased to 900 °C under an argon (Ar) atmosphere at a heating rate of 5 °C/min, followed by maintaining this temperature for 3 h with a cooling rate of 3 °C/min. The black powder sample is obtained by cooling it to room temperature. A 4 mol/L hydrochloric acid solution was added to 0.2 g of the black powder and stirred overnight on a magnetic stirrer for the purpose of removing the Zn element. Subsequently, the filtrate was washed with deionized water until it reached neutrality, and the filter residue was then subjected to drying at 60℃ in a blast dryer. The obtained black powder was designated as Co/N-PC.

The $Na_3V_2(PO_4)_2F_3$/Co/N-PC composites were synthesized through spray drying and high temperature sintering. A mixture of 2.3398 g NH_4VO_3, 2.3004 g $NH_4H_2PO_4$, 1.2597 g NaF, and an appropriate amount of citric acid was utilized as the reducing agents, followed by the addition of Co/N-PC. The aforementioned drugs were introduced into a round-bottom flask, and 30 mL of ultra-pure water was added as the solvent. The mixture was stirred in an oil bath at 80℃ for 6-8 hours until complete dissolution occurred. Subsequently, the $Na_3V_2(PO_4)_2F_3$/Co/N-PC precursor powder was obtained by passing the resulting solution through a spray dryer operating at 200℃. The $Na_3V_2(PO_4)_2F_3$/Co/N-PC precursor powder is subsequently transferred to an alumina crucible and subjected to high-temperature sintering in a tubular furnace under Ar gas protection. Initially, the $Na_3V_2(PO_4)_2F_3$/CO/N-PC precursor powder is heated at 300℃ for 3 h (heating rate: 5℃/min). Subsequently, the sample is calcined at 650℃ for 6 h (heating rate: 10℃/min), followed by natural cooling to room temperature. Consequently, the $Na_3V_2(PO_4)_2F_3$/Co/N-PC cathode material is obtained.

This preprint research paper has not been peer reviewed. Electronic copy available at: https://ssrn.com/abstract=5014891

The $Na_3V_2(PO_4)_2F_3$/N-PC composites were prepared in accordance with the previous methodology[26].

2.2 Material characterization

The X'Pert3 Powder-DY5103 multifunctional X-ray diffractometer (XRD, Panacor, Netherlands) equipped with a Cu target and λ=1.54056 Å was utilized for qualitative and quantitative analysis of phases as well as structure determination. The material microstructure was examined using a field emission scanning electron microscope (FESEM) (SU5000, Hitachi, Japan), equipped with both a secondary electron detector and a backscatter detector. In addition, energy dispersion spectroscopy (EDS) was employed for analysis. The valence states of elements in material samples were analyzed using X-ray photoelectron spectroscopy (XPS) with a Thermo Scientific K-Alpha spectrometer. The particle size, surface area, pore volume, and pore diameter of the sample were determined using the static volumetric method with BET analysis (V-Sorb 2800TP) provided by Beijing Jin Aipu Technology Co., Ltd.

2.3 Electrode and battery preparation

A mixture comprising 70 wt% $Na_3V_2(PO_4)_2F_3$/N-PC, 20 wt% acetylene black, and 10 wt% CMC was prepared by thoroughly mixing and grinding the three components in an agate mortar. Ultra-pure water was gradually added drop by drop while continuing to mix and grind until a slurry with no graininess was obtained. The resulting slurry sample was uniformly coated onto aluminum foil and subsequently transferred to a vacuum drying oven for a duration of 12 h. The diaphragm was composed of glass fiber, while the electrolyte consisted of a 1 M $NaClO_4$ vinyl carbonate (EC) Propylene carbonate (PC) solution with a 5 wt% addition of vinyl fluorocarbonate (FEC) in a volume ratio of 1:1. The half cell is assembled within an argon-filled glove box featuring a controlled environment with extremely low levels of oxygen and water content (O_2 < 0.01 ppm, H_2O < 0.01 ppm).

2.4 Electrochemical test

After being subjected to a 12 h standing period, the prepared battery underwent charging and discharging processes at various current densities within the voltage range of 2.3-4.7 V using the Neware battery charging and discharging system. Additionally, the rate capability tests was conducted

5

on the charge and discharge system, employing rates of 0.1 C, 0.2 C, 0.5 C, 1 C, and 2 C. The cyclic voltammetry (CV) measurements were conducted using a CHI760D electrochemical workstation at a scanning rate of 0.1 mV/s and within a voltage range of 2.3-4.7 V. Electrochemical impedance spectroscopy (EIS) was performed on an electrochemical workstation, employing a frequency range from 10^{-2} to 10^{-6} Hz and an amplitude of 5 mV.

3 Result and discussion

### 3.1 Physical characterization of $Na_3V_2(PO_4)_2F_3$/Co/N-PC composites.

In order to substantiate the suitability of the powder material prepared in Section 2.1 as a bimetallic MOF material, XRD analysis of the powder material is presented in Fig. 1. It can be observed from Fig. 1 that the characteristic peaks of the synthesized powder material closely resemble those simulated by crystal data for ZIF-8 and ZIF-67. These results unequivocally demonstrate successful synthesis of well-crystallized Co/Zn-ZIF bimetallic MOF material using a natural sedimentation method.

The results of the $Na_3V_2(PO_4)_2F_3$/Co/N-PC composite with 5 wt% carbon content, as shown in Fig. 1.(b), were refined using fullprof. The material exhibits a P42/mnm tequartet structure, which is consistent with the literature on $Na_3V_2(PO_4)_2F_3$[27-29]. After fitting, the cell parameters are a = 9.038 Å, b = 9.038 Å, c = 10.737 Å, and the cell volume is 877.06 Å³, indicating that the volume of $Na_3V_2(PO_4)_2F_3$ material decreases after modification with bimetallic MOF-derived carbon. This reduction in volume enhances its suitability for ion transport and deembedding.
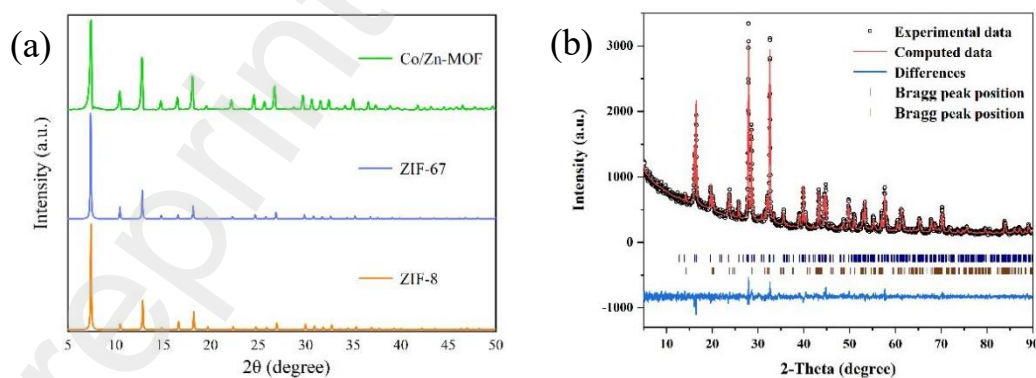
Fig. 1 (a) Comparison of XRD patterns of metal MOF, and (b) Results of refined $Na_3V_2(PO_4)_2F_3$/Co/N-PC composite with 5 wt% carbon content using fullprof

The microscopic morphology of Co/N-PC at different magnifications is depicted in Fig. 2(a)-(b). It can be visually observed that the Co/N-PC synthesized in this study exhibits a nanocube structure, thereby enhancing surface roughness and increasing the specific surface area, which aligns with previous findings reported in literature[27]. The microstructure analysis in Fig. 2(c)-(d) reveals the hollow sphere structure of the Co/N-PC-modified $Na_3V_2(PO_4)_2F_3$/Co/N-PC material, with numerous small nanocube structures (Co/N-PC) attached on both its surface and interior. This unique architecture enhances material conductivity and increases specific surface area, thereby mitigating capacity decay resulting from microstructural collapse during repeated charge-discharge cycles.
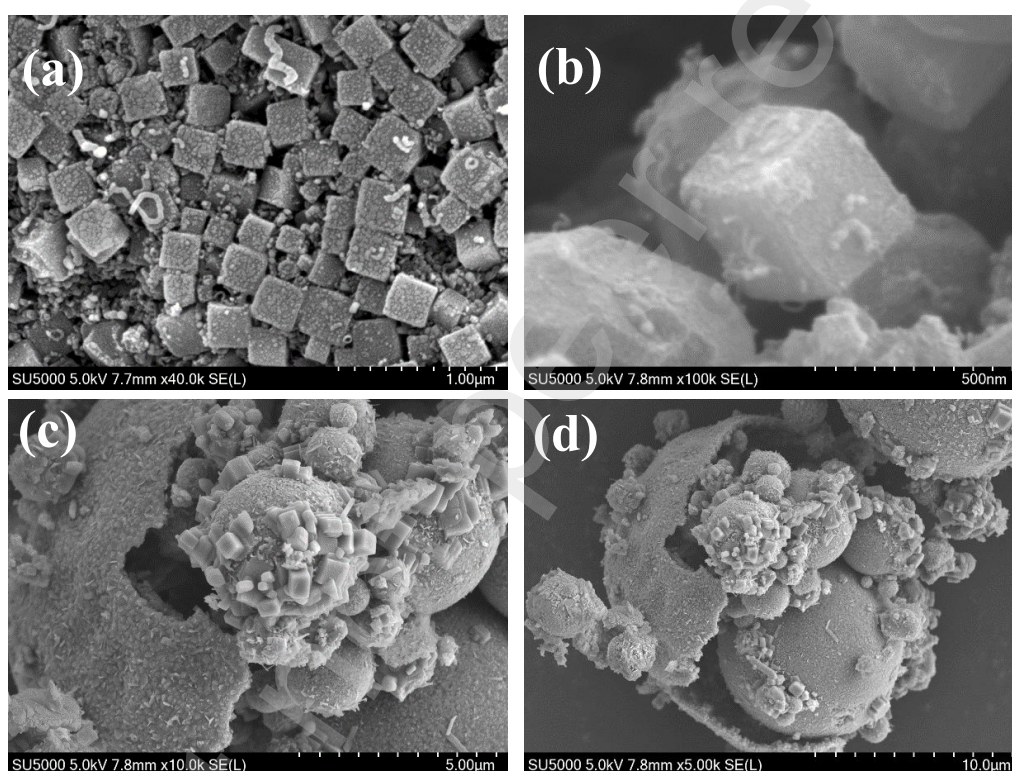
Fig.2 (a-b) SEM diagram of bimetallic MOF derived carbon at different multiples, and (c-d) SEM diagram of $Na_3V_2(PO_4)_2F_3$/Co/N-PC composite material at different multiples

The $Na_3V_2(PO_4)_2F_3$/Co/N-PC composite material was synthesized and characterized using EDS analysis and XPS energy spectrum analysis, following the experimental methodology described in Section 2.1. A comprehensive investigation and summary of the elemental composition of the material, as well as the chemical valence state of vanadium, were conducted. The corresponding results are presented in Fig. 3.
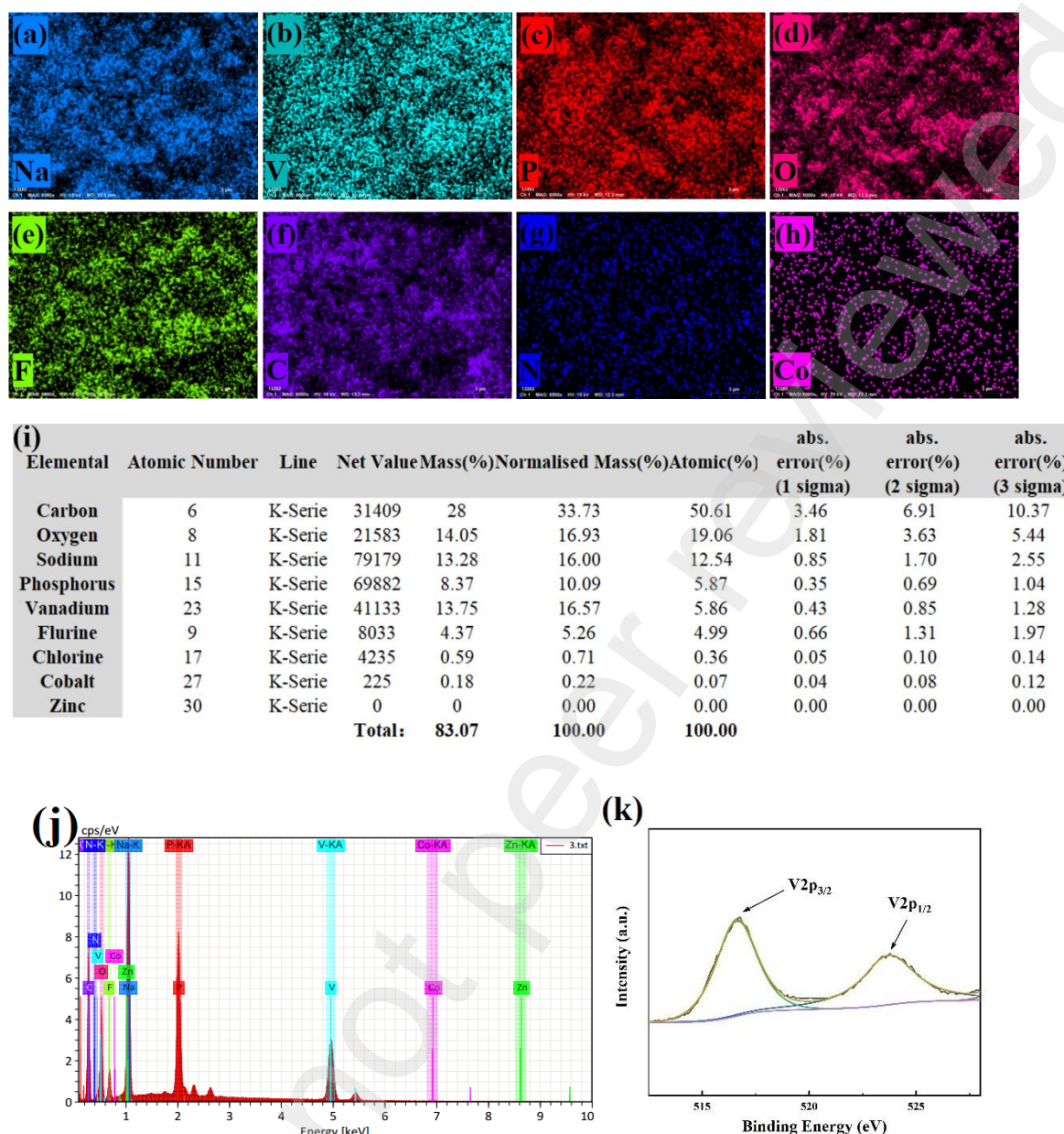
Fig.3 (a-h) EDS distribution diagram, (i) element content diagram, (j) element energy ratio EDS diagram, and (k) XPS diagram of $Na_3V_2(PO_4)_2F_3$/Co/N-PC composite material

The EDS spectra in Fig. 3(a) and Fig. 3(h)-(j) demonstrate the presence of all elements within the $Na_3V_2(PO_4)_2F_3$/Co/N-PC composites, with clear visibility of the mapping distribution for each element. Furthermore, a uniform distribution of C and N elements is observed in the prepared $Na_3V_2(PO_4)_2F_3$/Co/N-PC composite, indicating homogeneous dispersion of carbon-modified materials using the method described in this paper. The total content of each element in Fig. 3(i) amounts to 100%, indicating the absence of any miscellaneous elements in the material. All elements and their corresponding contents are consistent with those present in the material. Additionally, the EDS test

8

includes analysis of Zn element, but as shown in Fig. 3(i), its content is observed to be zero, suggesting that residual Zn metal has been effectively eliminated through excess HCl treatment Fig. 3(k) displays the XPS photoelectron spectra of $Na_3V_2(PO_4)_2F_3$/Co/N-PC composites. The obtained data was analyzed with Avantage software, indicating the existence of two distinct V element peaks around 516.7 eV and 523.7 eV. The observed phenomenon can be attributed to a self-selected orbital splitting between $V2p_{3/2}$ and $V2p_{1/2}$. The statement aligns with the V^{3+} binding energy documented in the literature[30].

The $Na_3V_2(PO_4)_2F_3$/Co/N-PC composites were subsequently subjected to specific surface area (BET) testing, and the corresponding results are illustrated in Fig. 4: the BET surface area of the $Na_3V_2(PO_4)_2F_3$/Co/N-PC composite is 21.107 m^2/g, with an average pore size of 7.170 nm as measured by the BJH method. This represents a significant improvement over the pure $Na_3V_2(PO_4)_2F_3$ material (1.365 m^2/g) and the $Na_3V_2(PO_4)_2F_3$/N-PC composite (5.100 m^2/g)[26]. The $Na_3V_2(PO_4)_2F_3$/Co/N-PC composites demonstrate a significantly enhanced specific surface area, accompanied by an increased number of active reaction sites, which aligns with the findings presented in Fig. 2.
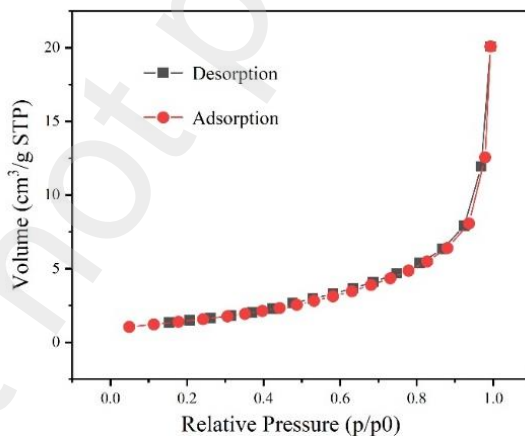

Fig. 4 Adsorption and desorption curve of $Na_3V_2(PO_4)_2F_3$/Co/N-PC composite

The XRD patterns of $Na_3V_2(PO_4)_2F_3$/N-PC and $Na_3V_2(PO_4)_2F_3$/Co/N-PC cathode materials after various charge and discharge cycles are presented in Fig. 5 (a)-(b). The XRD pattern reveals that the diffraction peak position remains unaffected by the capacity attenuation after multiple charge and discharge cycles, indicating that the crystal structure of the electrode material itself remains intact despite an increase in cycle number. At low cycle times, The capacity attenuation of the cathode materials in both sodium-ion batteries is not necessarily correlated with the crystal structure.

9
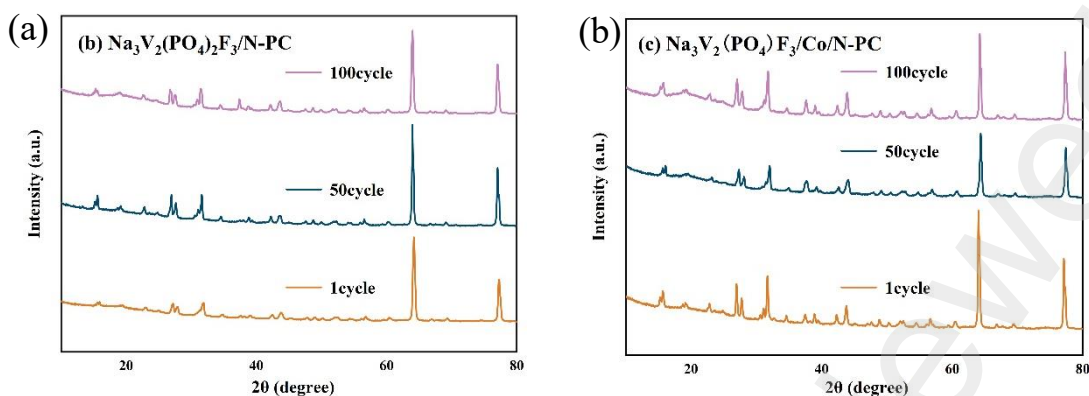
Fig. 5 XRD patterns of (a) $Na_3V_2(PO_4)_2F_3$/N-PC composite materials, (b) $Na_3V_2(PO_4)_2F_3$/Co/N-PC composite materials under different cycles
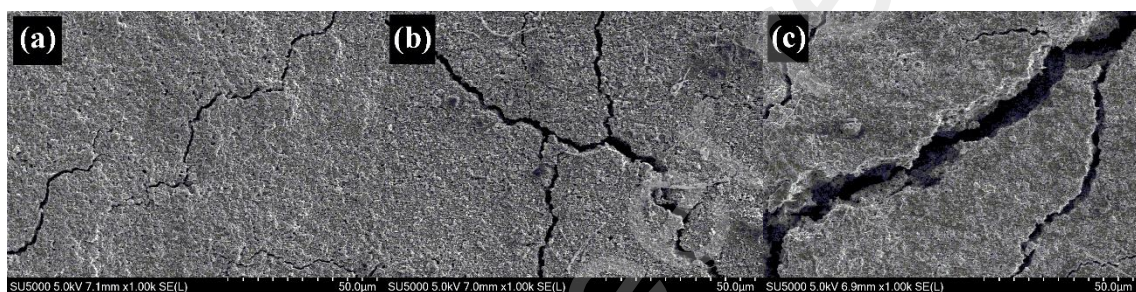
Fig. 6 SEM images of $Na_3V_2(PO_4)_2F_3$/Co/N-PC at (d) 1st, (e) 50th, and (f) 100th cycles

The morphology of the positive electrode material $Na_3V_2(PO_4)_2F_3$/Co/N-PC after 1, 50, and 100 charge and discharge cycles is depicted in Fig. 6(a)-(c), respectively. After grinding and coating with a conductive agent, acetylene black, binder CMC, and ultra-pure water, followed by completing a full charge-discharge process under electrolyte conditions, the figure does not exhibit an evident hollow sphere structure. This absence can be attributed to the transfer of the hollow sphere structure through ion exchange in the electrolyte after electrification, resulting in corrosion and exhibiting the morphology depicted in Fig. 6, Moreover, following electrification, the particles undergo polymerization in the micromorphology as a result of the Coulombic attraction between charges. The microstructure of the materials exhibited increasingly severe agglomeration and cracking phenomena, as depicted in Fig. 6(a)-(c). Particularly in Fig. 6(c), a significant area of adhesion and agglomeration was observed, resulting in a reduction in the material's specific surface area, available active sites for reaction, and ion deincarceration channels. This phenomenon constitutes an irreversible factor contributing to the attenuation of battery capacity.

10

The FT-IR images of $Na_3V_2(PO_4)_2F_3$/N-PC and $Na_3V_2(PO_4)_2F_3$/Co/N-PC electrode materials at different cycles are depicted in Fig. 7.
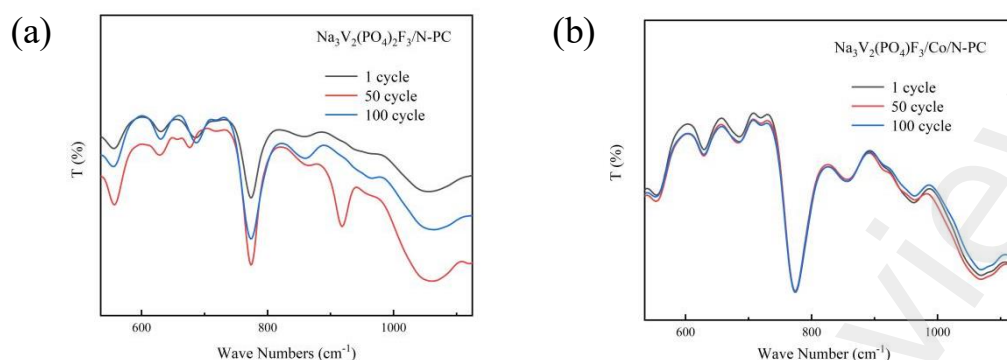
Fig. 7 FT-IR Chart of two electrode materials under different cycle times (a) $Na_3V_2(PO_4)_2F_3$/N-PC, (b) $Na_3V_2(PO_4)_2F_3$/Co/N-PC

The infrared absorption peaks of the two materials in Fig. 7 are observed to occur within the same range, and their positions align closely. This observation further supports that the characteristic functional groups of $Na_3V_2(PO_4)_2F_3$ modified materials remain unchanged regardless of the number of charge-discharge cycles and capacity attenuation is not directly associated with alterations in functional groups. As shown in Fig. 7, the V-O bonds are represented by the two peaks at 916 cm^{-1} and 635 cm^{-1}, while the asymmetric stretching vibration of the middle P-O bond is indicated by a single peak in the range of 1000-1100 cm^{-1}. Additionally, the symmetric stretching vibration of the P-O bond and bending vibration are observed at 681 cm^{-1} and 567 cm^{-1} respectively. These findings align with previous literature reports [31].

The XRD and FT-IR results revealed minimal alterations in the crystal structure and functional groups of the two electrode materials throughout various charge and discharge cycles. However, SEM analysis demonstrated that the cycling process significantly impacted the microstructure of the material, resulting in irreversible capacity attenuation within the battery. Importantly, it was discovered that neither functional groups nor crystal structure were primarily accountable for this capacity decay at low cycle times. Instead, it was observed that agglomeration and deposition of electrode material microstructure on the negative electrode surface played a pivotal role in inducing irreversible phenomena associated with capacity attenuation.
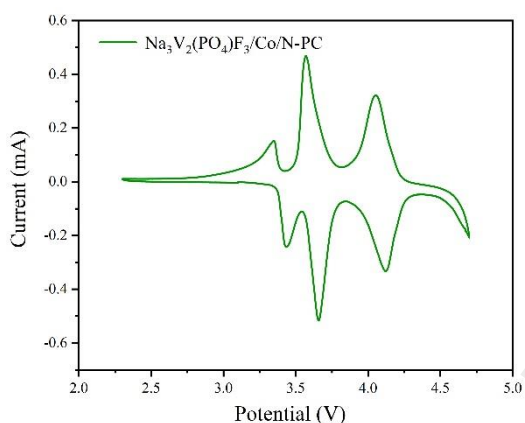
3.2 Electrochemical test of $Na_3V_2(PO_4)_2F_3$/Co/N-PC composites material

The composite $Na_3V_2(PO_4)_2F_3$/Co/N-PC, obtained by modifying $Na_3V_2(PO_4)_2F_3$ with bimetallic

11

MOF-derived carbon (Co/N-PC), was subjected to cyclic voltammetric scanning tests. The voltage range for the test was set at 2.3-4.7 V, and the scanning speed was maintained at 0.1 mV/s. The results are presented in Fig. 8.

The voltage range of 2.3-4.7 V exhibits three pairs of REDOX peaks during the charge and discharge process of the electrode material, as illustrated in Fig. 8. This observation suggests that the material undergoes three Na^+ displacements, with oxidation peaks occurring at positions of 3.35 V, 3.57 V, and 4.05 V respectively, while reduction peaks are located at 3.44 V, 3.66 V, and 4.12 V correspondingly. Importantly, the small peak voltage difference ΔEp between each pair of REDOX peaks confirms excellent reversibility in the electrode reaction. The electrochemical properties of composites modified with Co/N-PC exhibit superior performance compared to that of the pristine phase materials in $Na_3V_2(PO_4)_2F_3$/Co/N-PC. The active site of Co nanoparticles embedded in the nanocubes facilitates charge transfer in carbon materials, while N doping shortens the ion deincarceration channel. The synergistic effect of these two factors contributes to the excellent electrochemical performance of $Na_3V_2(PO_4)_2F_3$/Co/N-PC composites. Simultaneously, the presence of three pairs of redox peaks in the CV diagram indicates that the deintercalation of sodium ions from $Na_3V_2(PO_4)_2F_3$/Co/N-PC composite during a charge-discharge cycle occurs at three distinct sites, suggesting the existence of three Na^+ deintercalation sites. According to the reaction mechanism of $Na_3V_2(PO_4)_2F_3$ electrode, these three pairs of redox peaks may correspond to three reversible reactions involving

$$Na_3V_2(PO_4)_2F_3 \rightleftharpoons Na_2V_2(PO_4)_2F_3^- + Na^+ \qquad (1)$$

$$Na_2V_2(PO_4)_2F_3^- \rightleftharpoons NaV_2(PO_4)_2F_3^{2-} + Na^+ \qquad (2)$$

$$NaV_2(PO_4)_2F_3^{2-} \rightleftharpoons V_2(PO_4)_2F_3^{3-} + Na^+ \qquad (3)$$

This preprint research paper has not been peer reviewed. Electronic copy available at: https://ssrn.com/abstract=5014891

Fig. 8 CV Curve of $Na_3V_2(PO_4)_2F_3$/Co/N-PC Composite in 2.3-4.7 V

The $Na_3V_2(PO_4)_2F_3$/Co/N-PC composite exhibits a consistently high specific discharge capacity at various magnifications, as depicted in Fig. 9(a). At a rate of 0.1 C, the specific capacity reaches 126.66 mAh/g, and distinct plateaus are observed during cyclic charging and discharging at higher magnifications. These plateaus correspond to the three pairs of REDOX peak voltages illustrated in Fig. 8. Compared with $Na_3V_2(PO_4)_2F_3$/N-PC, the specific capacity of $Na_3V_2(PO_4)_2F_3$/Co/N-PC composite is increased by 15.6%. As illustrated in Fig. 9(b), when the replacement rate causes the transition of $Na_3V_2(PO_4)_2F_3$/Co/N-PC composite material from 0.1 C to 2 C and eventually back to 0.1 C, its specific discharge capacity closely approximates the initial discharge specific capacity at 0.1 C. It is also indicates that the material has an excellent cycling stability.
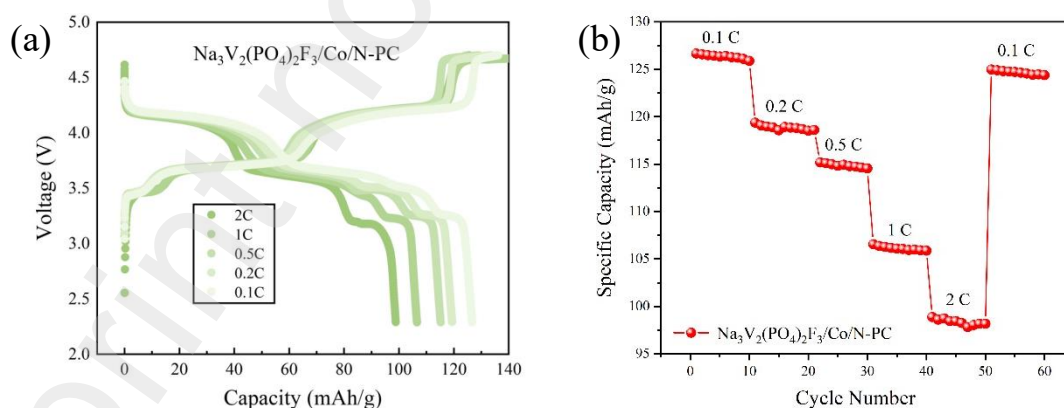
Fig. 9 (a) Charge discharge curves and (b) magnification performance of $Na_3V_2(PO_4)_2F_3$/Co/N-PC composite materials at different magnification

The electrochemical impedance spectroscopy test results for $Na_3V_2(PO_4)_2F_3$/Co/N-PC composites modified with bimetallic MOF-derived carbon are presented in Fig. 10, along with the

13

corresponding equivalent circuit. Table 1 shows the fitted impedance parameters.
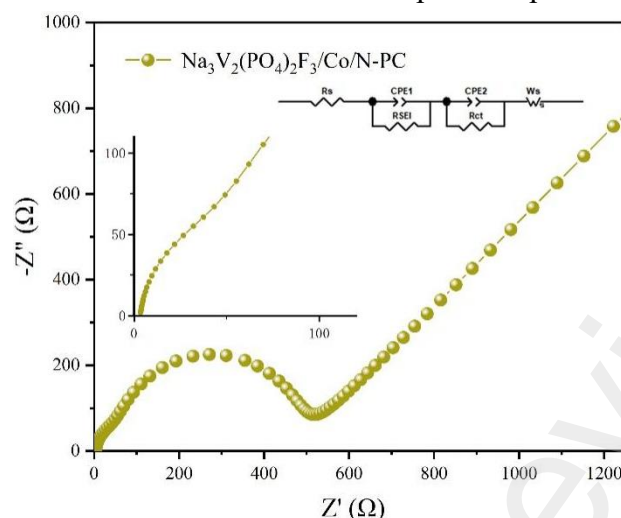
Fig. 10 EIS Diagram of $Na_3V_2(PO_4)_2F_3/Co/N$-PC Composite

Table 1

Electrochemical impedance spectroscopy parameter table.

Material type	R_s (Ω)	R_{SEI} (Ω)	R_{ct} (Ω)
$Na_3V_2(PO_4)_2F_3/Co/N$-PC	3.02	48.62	457.1
$Na_3V_2(PO_4)_2F_3/N$-PC	8.067	81.55	527.1

The impedance diagram of the $Na_3V_2(PO_4)_2F_3/Co/N$-PC composite, as shown in Fig. 10, exhibits three distinct components: two arcs representing the high and middle frequency regions, along with oblique lines indicating the low frequency regions. The semicircular impedance observed in the high frequency region can be attributed to the presence of a SEI film at the electrode/electrolyte interface, while the combination of a semicircle and a straight line in the middle and low frequency regions is indicative of charge transfer resistance. The numerical value of R_{SEI} is 48.62 Ω, which is smaller than that of the $Na_3V_2(PO_4)_2F_3/N$-PC composite, The results indicate that the modified material of bimetallic MOF-derived carbon exhibits enhanced permeability across the SEI membrane interface, which is consistent with its superior electrochemical performance compared to $Na_3V_2(PO_4)_2F_3/N$-PC composites.

The EIS spectra of the two electrode materials are presented in Fig. 11, depicting the results obtained from charging and discharging cycles with varying numbers of turns on the Neware battery

14

test system at room temperature. A three-electrode configuration consisting of a positive electrode sheet as the working electrode, a sodium ring as the reference electrode, and a sodium sheet as the opposite electrode was employed. The voltage range was set at 2.3-4.7 V. Subsequently, batteries with varying cycle numbers were detached and connected to an electrochemical workstation for EIS testing. The resulting Nyquist plot was obtained.After assembling the three-electrode device in an argon-filled glove box, it should be removed and allowed to equilibrate at room temperature for 30 minutes prior to powering on for testing.

The impedance diagram in Fig. 11 reveals that during the initial charge and discharge cycles of the two electrode materials, the high frequency region associated with the SEI film formed at the electrode/electrolyte interface exhibits a larger semi-circle compared to that observed in the cyclic multi-loop impedance diagram. Throughout the progression from the initial circle to the 100th circle, it is evident that there is a gradual reduction in size for the semi-circle representing the high-frequency region of the impedance diagram. This observation, when combined with data from Table 2, reveals a progressive decline in R_{SEI} as cycle number increases, indicating a diminishing hindrance for ion passage through the SEI film within 100 cycles. Consequently, this fundamental phenomenon elucidates why the battery retains substantial capacity even after numerous cycles. In principle, the formation of the SEI film occurs during the initial release of sodium ions upon the first charge and discharge cycles of the battery. This irreversible process is crucial, and the presence of SEI film positively influences ion release. Although the formation of the film necessitates the consumption of a portion of sodium ions, resulting in a reduced availability of sodium ions for deembedding within the system, it also establishes a pathway for subsequent deembedding of sodium ions. However, with repeated charging and discharging cycles, the SEI film gradually thickens as the number of cycles increases. During low cycle counts (less than 100 cycles), this increased thickness still positively facilitates ion deembedding. Despite a gradual decrease in R_{SEI} throughout the process, the SEI film thickens with an increasing number of cycles, resulting in the consumption of Na^+ utilized for deembedding within the system. Consequently, this phenomenon accounts for both the diminishing R_{SEI} values and a continuous decline in capacity[32].
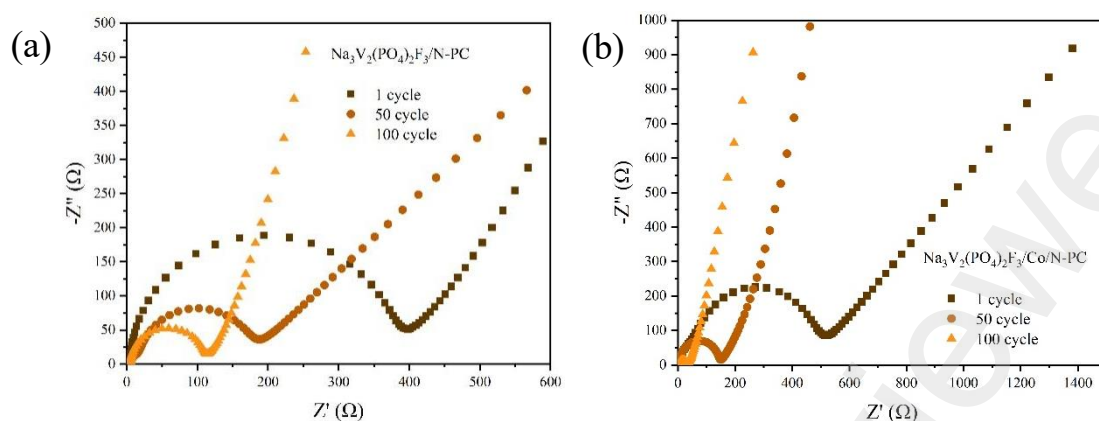
Fig. 11 EIS Chart of three electrode materials under different cycle times (a) Na$_3$V$_2$(PO$_4$)$_2$F$_3$/N-PC, (b) Na$_3$V$_2$(PO$_4$)$_2$F$_3$/Co/N-PC
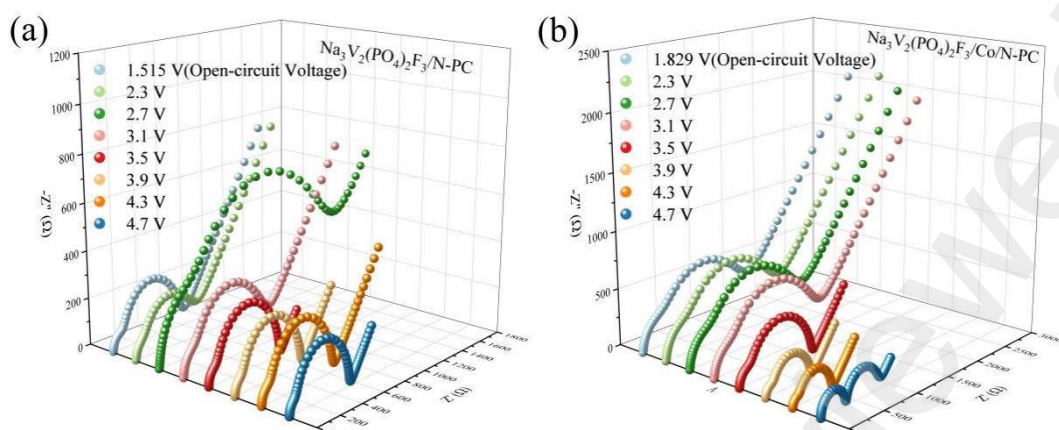
Table 2

R_{SEI} impedance values corresponding to three electrode materials at different cycles.

Materials	Number of cycles	R_{SEI}/Ω
Na$_3$V$_2$(PO$_4$)$_2$F$_3$/N-PC	1	362.8
—	50	148.9
—	100	101.1
Na$_3$V$_2$(PO$_4$)$_2$F$_3$/Co/N-PC	1	137.1
—	50	45.71
—	100	26.48

The experiment demonstrates that after numerous cycles, the thickness of the SEI film will eventually impede ion removal, thereby hindering its functionality. Consequently, it is anticipated that the semi-circle associated with the high-frequency region in the EIS plot will once again exhibit an enlarged magnitude[33].

The Nyquist diagram of the initial charging process for the two electrode materials at ambient temperature is depicted in Fig. 12. The initial voltage corresponds to the open circuit voltage of all three electrodes, while the cut-off voltage is set at 4.7 V.

16

Fig. 12 Nyquist diagram of three electrode materials during charging process (a) Na$_3$V$_2$(PO$_4$)$_2$F$_3$/N-PC, (b) Na$_3$V$_2$(PO$_4$)$_2$F$_3$/Co/N-PC

Table 3

Corresponding impedance values of two electrode materials at different voltages during the first charging process.

material	voltage/V	R_s/Ω	R_{SEI}/Ω	R_{ct}/Ω
	1.515	8.828	83.55	478.1
	2.3	6.338	354.4	89.55
	2.7	5.928	421	75.5
Na$_3$V$_2$(PO$_4$)$_2$F$_3$	3.1	7.387	538.2	74.2
/N-PC	3.5	4.892	541.1	72.15
	3.9	9.504	537.1	72.02
	4.3	9.504	503	64.06
	4.7	7.387	469.2	53.67

material	voltage/V	R_s/Ω	R_{SEI}/Ω	R_{ct}/Ω
	1.829	4.008	243.2	1099
	2.3	3.944	270.2	1095.3
Na$_3$V$_2$(PO$_4$)$_2$F$_3$	2.7	3.776	279.8	1012
/Co/N-PC	3.1	4.031	285.2	899
	3.5	4.92	857.7	159.9
	3.9	5.001	521.7	101.5

17

4.3	4.808	451.3	88.55
4.7	5.315	346.4	452.4

In Fig. 12, this can be clearly observed the Nyquist diagrams at different voltages in the entire charging process clearly exhibit a high frequency region and a semicircle associated with the resistance of ions passing through the SEI film at the electrode/electrolyte interface, as well as a semicircle and a diffusion oblique line related to the charge transfer resistance in the middle and low frequency regions.

The combined analysis of the two figures in Fig. 12 and the two data tables in Table 3 indicates a negligible difference in liquid resistance (R_s) between the two electrode materials during the charging process, suggesting minimal impact on their electrochemical performance. However, it is worth noting that both electrode materials can obtain R_{SEI} values at any voltage, with $Na_3V_2(PO_4)_2F_3$/Co/N-PC exhibiting a lower R_{SEI} compared to $Na_3V_2(PO_4)_2F_3$/N-PC. The R_{ct} of $Na_3V_2(PO_4)_2F_3$/Co/N-PC exhibited an overall decreasing trend, indicating that the incorporation of carbon materials effectively mitigated electrolyte-induced damage to the positive electrode material, enhanced interface stability, and reduced interfacial charge transfer resistance. This demonstrates the feasibility of utilizing the exceptional structure of MOFs material and its transformation into carbon material for electrode material modification.

The data analysis in Table 3 reveals a distinct pattern of initial increase followed by subsequent decrease in the R_{SEI} values during the charging process of both electrode materials. The information depicted in Fig. 12 indicates that the electrode materials were charged at fixed intervals (every 0.4 V) subsequent to their initial voltage being elevated to 2.3 V. The R_{SEI} is observed to move in the direction away from the real axis while charging their respective initial voltage to 3.5 V, indicating an increase in the R_{SEI} value. The Nyquist diagram of the electrochemical impedance spectrum clearly illustrates variations in the semicircle associated with charge transfer resistance within the intermediate frequency range as voltage increases, indicating a decrease in R_{ct} value. This can be attributed to the enhanced electrochemical performance of the modified electrode material resulting from carbon material modification.

4 Conclusion

In summary, the bimetallic Co/Zn-ZIF material was synthesized using the solution heat method

and subsequently transformed into a nitrogen-doped derived carbon material containing Co(Co/N-PC) through high temperature pyrolysis. Furthermore, the $Na_3V_2(PO_4)_2F_3$/Co/N-PC composite was in situ generated by spray drying combined with high temperature calcination for subsequent investigation of its electrochemical properties. It was observed that Co/N-PC displayed a nano-cubic morphology, being attached to both exterior and interior surfaces of hollow spheres. This distinctive architecture led to an augmented specific surface area as well as increased reactive sites within the material. Furthermore, Co nanoparticles promoted charge transfer and improved conductivity in carbon materials. Moreover, incorporating nitrogen into this composite reduced Na^+ deintercalation pathway length, thus exerting a positive influence on its electrochemical performance. At a rate of 0.1 C, the initial specific discharge capacity of the composite reached 126.66 mAh/g and maintained 91.84% retention after 100 cycles. EIS analysis rcaevealed a lower resistance value at R_{SEI}, compared to $Na_3V_2(PO_4)_2F_3$/N-PC composite, facilitating ion exchange through the SEI membrane; specifically, an R_{SEI} value as low as 48.62 Ω contributed to its superior electrochemical performance.

Acknowledgments

Reference

[1]H. Lyu, J. Liu, S. Mahurin, S. Dai, Z. Guo, X. Sun, Polythiophene coated aromatic polyimide enabled ultrafast and sustainable lithium ion batteries, J. Mater. Chem. A. 5(46) (2017) 24083-24090.
[2]J. Zhao, T. Kang, Y. Chu, P. Chen, F. Jin, Y. Shen, L. Chen, A polyimide cathode with superior

stability and rate capability for lithium-ion batteries, Nano. Res, 12(6) (2019) 1355-1360.

[3] Y. Zhao, K. Kamiya, K. Hashimoto, S. Nakanishi, Hydrogen evolution by tungsten carbonitride nanoelectrocatalysts synthesized by the formation of a tungsten acid/polymer hybrid in situ, Angew Chem. Int. Ed. Engl, 52(51) (2013) 13638-13641.

[4] B. Cao, G. M. Veith, J. C. Neuefeind, R. R. Adzic, P. G. Khalifah, Mixed close-packed cobalt molybdenum nitrides as non-noble metal electrocatalysts for the hydrogen evolution reaction, J. Am. Chem. Soc, 135(51) (2013) 19186-19192.

[5] W. Chen, K. Sasaki, C. Ma, A. I. Frenkel, N. Marinkovic, J. T. Muckerman, Y. Zhu, R. R. Adzic, Hydrogen-evolution catalysts based on non-noble metal nickel-molybdenum nitride nanosheets, Angew. Chem. Int. Ed. Engl, 51(25) (2012) 6131-6135.

[6] C. Prior, L. R. Webster, S. K. Ibrahim, J. A. Wright, A. F. Alghamdi, V. S. Oganesyan, C. J. Pickett, EPR detection and characterisation of a paramagnetic Mo(iii) dihydride intermediate involved in electrocatalytic hydrogen evolution, Dalton.T, 45(6) (2016) 2399-2403.

[7] S. De, J. Zhang, R. Luque, N. Yan, Ni-based bimetallic heterogeneous catalysts for energy and environmental applications, Energy. Environ. Sci, 9(11) (2016) 3314-3347.

[8] C. Hu, L. Dai, Multifunctional Carbon-Based Metal-Free Electrocatalysts for Simultaneous Oxygen Reduction, Oxygen Evolution, and Hydrogen Evolution, Adv. Mater, 29(9) (2017) 1604942.

[9] L. Yu, H. B. Wu, X. W. Lou, Self-Templated Formation of Hollow Structures for Electrochemical Energy Applications, Acc. Chem. Res, 50(2) (2017) 293-301.

[10] Y. Cui, Y. Yue, G. Qian, B. Chen. Luminescent functional metal-organic frameworks, Chem. Rev, 112(2) (2012) 1126-1162.

[11] Z. Liang, R. Zhao, T. Qiu, R. Zou, Q. Xu. Metal-organic framework-derived materials for electrochemical energy applications, J. Energ. Chem, 1(1) (2019) 100001.

[12] Y. Liu, W. Xuan, Y. Cui, Engineering homochiral metal-organic frameworks for heterogeneous asymmetric catalysis and enantioselective separation, Adv. Mater, 22(37) (2010) 4112-4135.

[13] L. J. Murray, M. Dinca, J. R. Long, Hydrogen storage in metal-organic frameworks, Chem. Soc. Rev, 38(5) (2009) 1294-1314.

[14] Z. Pan, J. Xu, H. Zheng, K. Huang, Y. Li, Z. Guo, S. R. Batten, Three new heterothiometallic cluster polymers with fascinating topologies, Inorg. Chem, 48(13) (2009) 5772-5778.

[15] R. Wang, P. Sun, Q. Yuan, R. Nie, X. Wang, MOF-derived cobalt-embedded nitrogen-doped mesoporous carbon leaf for efficient hydrogen evolution reaction in both acidic and alkaline media, Int. J. Hydrogen. Energ, 44(23) (2019) 11838-11847.

[16] Z. Wang, Z. Jin, G. Wang, B. Ma, Efficient hydrogen production over MOFs (ZIF-67) and g-C_3N_4 boosted with MoS2 nanoparticles, Int. J, Hydrogen Energ, 43(29) (2018) 13039-13050.

[17] L. Xiong, J. Bi, L. Wang, S. Yang, Improving the electrocatalytic property of CoP for hydrogen evolution by constructing porous ternary CeO_2-CoP-C hybrid nanostructure via ionic exchange of MOF, International Journal of Hydrogen Energy, 43(45) (2018) 20372-20381.

[18] W. Zhang, R. G. Xiong. Ferroelectric metal-organic frameworks, Chem. Rev, 2012, 112(2): 1163-1195.

[19] D. Li, H. Xu, L. Jiao, H. Jiang, Metal-organic frameworks for catalysis: State of the art, challenges, and opportunities, J. Energ. Chem, 1(1) (2019).

[20] S. H. Oh, R. Black, E. Pomerantseva, J. H. Lee, L. F. Nazar. Synthesis of a metallic mesoporous pyrochlore as a catalyst for lithium-O_2 batteries, Nat. Chem, 4(12) (2012) 1004-1010.

[21] J. Zhao, H. Hu, M. Wu, N-Doped-carbon/cobalt-nanoparticle/N-doped-carbon multi-layer sandwich nanohybrids derived from cobalt MOFs having 3D molecular structures as bifunctional electrocatalysts for on-chip solid-state Zn-air batteries, Nanoscale, 12(6) (2020) 3750-3762.

[22] B. Chen, X. He, F. Yin, H. Wang, D. J. Liu, R. Shi, J. Chen, H. Yin, MO-Co@N-Doped Carbon (M = Zn or Co): Vital Roles of Inactive Zn and Highly Efficient Activity toward Oxygen Reduction/Evolution Reactions for Rechargeable Zn–Air Battery, Adv. Funct. Mater, 27(37) (2017).

[23] A. Zitolo, V. Goellner, V. Armel, M. T. Sougrati, T. Mineva, L. Stievano, E. Fonda, F. Jaouen, Identification of catalytic sites for oxygen reduction in iron- and nitrogen-doped graphene materials, Nat. Mater, 14(9) (2015) 937-942.

[24] Z. Xu, Y. Huang, C. Chen, L. Ding, Y. Zhu, Z. Zhang, Z. Guang. MOF-derived hollow $Co(Ni)Se_2$/N-doped carbon composite material for preparation of sodium ion battery anode, Ceram. Int, 46(4) (2020) 4532-4542.

[25] J. Yu, C. Mu, B. Yan, X. Qin, C. Shen, H. Xue, H. Pang, Nanoparticle/MOF composites: preparations and applications, Mater. Horiz, 4(4) (2017) 557-569.

[26] F. Zhou, W. Li, J. Ma, S. Wang, M. Lu, Z. Liu, G.-C. Han, Preparation of N-doped carbon-modified $Na_3V_2(PO_4)_2F_3$ based on ZIF-8 as a template and its electrochemical properties, Diam. Relat. Mater, (2024) 145.

[27] A. Criado, P. Lavela, G. Ortiz, J. L. Tirado, C. Pérez-Vicente, N. Bahrou, Z. Edfouf, Highly dispersed oleic-induced nanometric $C@Na_3V_2(PO_4)2F_3$ composites for efficient Na-ion batteries, Electrochimica. Acta, (2020) 332.

[28] Y. Li, X. Liang, G. Chen, W. Zhong, Q. Deng, F. Zheng, C. Yang, M. Liu, J. Hu, In-situ constructing $Na_3V_2(PO_4)_2F_3$/carbon nanocubes for fast ion diffusion with high-performance Na^+-storage, Chemical Engineering Journal, (2020) 387.

[29] Y. Mao, X. Zhang, Y. Zhou, W. Chu, Microwave-assisted synthesis of porous nano-sized $Na_3V_2(PO_4)_2F_3@C$ nanospheres for sodium ion batteries with enhanced stability, Scripta. Mater, 181 (2020) 92-96.

[30] M. C. Biesinger, B. P. Payne, A. P. Grosvenor, L. W. M. Lau, A. R. Gerson, R. S. C Smart, Resolving surface chemical states in XPS analysis of first row transition metals, oxides and hydroxides: Cr, Mn, Fe, Co and Ni, Appl. Surf. Sci, 257(7) (2011) 2717-2730.

[31] Z. Gu, J. Guo, Z. Sun, X. Zhao, W. Li, X. Yang, H. Liang, C. Zhao, X. Wu, Carbon-coating-increased working voltage and energy density towards an advanced $Na_3V_2(PO_4)_2F_3@C$ cathode in sodium-ion batteries, Sci. Bull, 65(9) (2020) 702-710.

[32] P. M. Attia, W. C. Chueh, S. J. Harris, Revisiting the t0.5 Dependence of SEI Growth, J Electrochem.Soc, 167(9) (2020) 090535.

[33] M. Lu, R. Guo, W. Li, Y. Lv, F. Tang, W. Feng, Z. Liu, G. Han, Z. Zhan, Interfacial characteristics of Na_2FePO_4F and its carbon coated material for lithium/sodium hybrid ion battery, J. Electroanal. Chem, 922 (2022) 116772.